

Fabrication of Nanostructured Electrodes for Biosensing and Energy Applications using Ni-Co Functional Inks

A Thesis submitted by
Urgunde Ajay Bhimashankar

in partial fulfillment of the requirements for the award of the degree of
Doctor of Philosophy

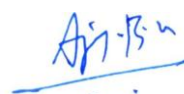


॥ त्वं ज्ञानमयो विज्ञानमयोऽसि ॥

Indian Institute of Technology Jodhpur
Chemistry
May 2021

Declaration

I hereby declare that the work presented in this thesis titled *Fabrication of Nanostructured Electrodes for Bio-sensing and Energy Applications using Ni-Co Functional Inks* submitted to Indian Institute of Technology Jodhpur in the partial fulfilment of the requirements for the award of the degree of Doctor of Philosophy, is a bonafide record of the research work carried out under the supervision of Professor Ritu Gupta. The contents of this thesis in full or in parts have not been submitted to, and will not be submitted by me to, any other Institute or University in India or abroad for the award of any degree or diploma.



Urgunde Ajay Bhimashankar
P16CY002

Certificate

This is to certify that the thesis titled *Fabrication of Nanostructured Electrodes for Bio-sensing and Energy Applications using Ni-Co Functional Inks*, submitted by Urgunde Ajay Bhimashankar (P16CY002) to the Indian Institute of Technology Jodhpur for the award of the degree of *Doctorate of Philosophy* is a bonafide record of the research work done by him under my supervision. To the best of my knowledge, the contents of this report, in full or in parts, have not been submitted to any other Institute or University for the award of any degree or diploma.



Ritu Gupta
Ph.D. Thesis Supervisor

Acknowledgements

I thank my Ph.D. Thesis supervisor, Professor Ritu Gupta, for her continuous support and encouragement. I offer my sincere appreciation for the learning opportunity provided by her in moulding me to go beyond my limits and dream for the best. I am grateful for her help, patience and constant reminders to be perfect in the little things that I do each day. I thank her for the life lessons, which helped me to overcome the tough times during the doctoral program. It is not only the life lessons that I have learned but to care, share and help those in need.

I sincerely thank Professor Rakesh Sharma and Dr. Pragati Sharma for their kind support. I would also like to thank all the professors from the Chemistry Department and IIT Jodhpur for guiding me and helping me with the course work. I thank the technical and non-technical staffs of the Chemistry Department, SAIF, and IIT Jodhpur for helping me with the equipment and other non-technical problems. I would also thank SAIF, Department of Chemistry, and IIT Jodhpur for providing access to the equipment, chemicals, and software facilities.

I thank Professor G. U. Kulkarni (JNCASR) for his constant motivational support and encouragement. I would also like to extend my gratitude towards my previous mentors Professor S. Murgavelh (VIT Vellore), Professor R. W. Gaikwad (PREC, University of Pune) and Professor V. G. Pangarkar.

I thank Gaurav Bahuguna for his support and help throughout my doctoral work. I would also like to thank Dr. Kiran Shejale, Dr. Devika Laishram, Dr. Krishanpriya (Chechi), Dr. Poonam Sharma, Dr. Vikas Janu, Dr. Puraram, Mohit, Anandita, Parijat, Snehraj, Vinod, Vipin, Akshay, Chesta, Hamid, Savi, Shailesh, Vikas and Arpit for making my stay at IIT Jodhpur memorable.

I am thankful to Nisha, Anandita, Mohit and Snehraj for sparing their valuable time for proof-reading the thesis. My stay at the Institute was a wonderful experience because of my friends Abhishek, Sheeba, Purva, Nisha, Shreya, Sonia, Rohit, Laxmikant, and Sourav for all the liveliness they infused into the non-academic part of the days at IIT Jodhpur.

My friends outside campus, Mahesh Dan, Ganesh, Priyanka, Rajneesh, Vikas, Swapnil, Dr. Vidyasagar, Dr. Anju, Sumair, and Revat Dan (Ravi), for making me believe I can surpass the tough times and taking good care of me besides my family when needed.

Finally, I acknowledge and thank my relatives for the patience and love they had for me. I also thank them for bearing with me when I could not spend much time with them. I would have been stronger without my mom, dad and my aunt. They are the inspiration which kept me thriving, pushing, facing all the struggles, pain and the hardships. I pay respects to my grandparents for all their love, sacrifices, and blessings. I would also like to thank my beloved sister Dr. Anjali Urgunde-Patil and Patil family for believing in me and not getting angry at times for not being with them when they needed me the most.

I whole-heartedly dedicate this thesis to my family!

Urgunde Ajay Bhimashankar
Ph.D. Student

List of Figures

Figures	Title	Page no.
1.1	Schematic representing the increased surface area to same volume of a cube.	1
1.2	(a) Schematic showing Oxygen Evolution Reaction (OER) in KOH electrolyte (b) Importance of oxides for OER.	3
1.3	A schematic of charging and discharging of a EDLC supercapacitor.	5
1.4	(a) Activated chemisorption model and (b) Incipient hydrous oxide adatom mediator model.	7
1.5	Literature reports of various techniques (a) hydrothermal (b) chemical bath sonication (c) radiofrequency sputtering (d) electrodeposition used in the fabrication of electrodes for glucose sensing.	10
1.6	Various materials explored for OER in literature reports (a) Nickel oxide (b) Cobalt monophosphosulfide (c) Cobalt phosphide and (d) Cobalt oxide.	12
1.7	Nickel cobaltite nanoplates synthesized using hydrothermal methods for application in (a) photoelectric and catalytic applications and (b) OER.	13
1.8	Materials like (a) MnO ₂ Nanowires (b) TiO ₂ graphene Composite (c) Graphene-Zinc oxide composite and (d) MgO Nanostructures with their corresponding electrochemical responses.	17
1.9	Different methods used for the synthesis of graphitic carbon (a) sealed high-pressure reactor, (b) Non-templated pyrolysis (c) Friedel-craft reaction with high temp annealing (d) Silica templated carbonization.	19
2.1	Potential waveforms for linear sweep (a) and (b) the corresponding voltammogram.	27
2.2	Potential waveforms for cyclic sweep (a) and (b) the corresponding voltammogram.	27
2.3	(a) Potential-excitation signals for NPV and its (b) corresponding voltammogram.	29
2.4	(a) Potential-excitation signals for DPV and its (b) corresponding voltammogram.	29
2.5	(a) Potential-excitation signals for SWV and its (b) corresponding voltammogram.	30
2.6	A typical Nyquist plot (Z' versus Z'') from EIS spectroscopy.	30
2.7	Photograph of (a) Au plain and (unpatterened) (b) patterned Au mesh electrode used as working electrodes.	35
3.1	Flexible sensors for glucose detection.	37
3.2	Characterization of Ni alkanethiolates of different chain lengths by FTIR spectroscopy.	39
3.3	Characterization of Ni alkanethiolates of different chain lengths by UV-visible spectroscopy.	40
3.4	(a) Fabrication of working electrode for electrochemical measurements. (b) FESEM image of the electrode after electro-oxidation.	40
3.5	CV measurements of blank Au film in 0.1 M NaOH (a) for 25 cycles at 50 mV/s and (b) with increasing scan rates.	41
3.6	CV scans for the first consecutive 25 cycles for Ni alkanethiolates, Ni(SR) ₂ , where R = (a) C ₄ H ₉ , (b) C ₈ H ₁₇ , (c) C ₁₂ H ₂₅ and (d) C ₁₆ H ₃₃ respectively in 0.1 M NaOH solution. Insets in each section show corresponding peak voltage variations with respect to the number of cycles. (e) Electrochemical behavior of Ni(SR) ₂ complexes (R= C ₄ H ₉ , C ₈ H ₁₇ , C ₁₂ H ₂₅ and C ₁₆ H ₃₃) at 50 mV/s after electro-oxidation step. (f) Anodic and cathodic peak current density with respect to the number of carbon atoms in the Ni(SR) ₂ .	41
3.7	Survey spectra (a) High Resolution XPS spectra of (b) S 2p, (c) Ni 2p and (d) O 1s in Ni-BT/Au electrode before and after electro-oxidation.	42
3.8	Electrochemical properties of Ni-BT/Au as a working electrode. (a and b) CV scans of Ni-BT/Au with and without glucose (1 mM) at different scan rates of 50 and 100 mV/s respectively (c and d) without and with 1 mM glucose (scan	43

	rates 10 – 300 mV/s). The relation between anodic and cathodic peak current with respect to scan rates (e) in 0.1 M NaOH (f) 1 mM glucose.	
3.9	(a) Fabrication of Au mesh functionalized with Ni-BT (b) Photographs of Au film and Au metal mesh electrodes. The letters below the electrode are clearly visible through the mesh network. (c) The transmittance spectra of Ni(SR) ₂ coated on Au film, FTO and Au mesh based electrodes.	44
3.10	(a-d) FESEM images of the crack network at different magnifications.	45
3.11	(a and b) CV measurements of Ni-BT/Au film and Ni-BT/Au mesh as working electrode at a scan rate of 50 mV/s.	45
3.12	Relationship between peak current and scan rate for Au mesh electrodes (a) in 0.1 M (Blank) NaOH (b) 1 mM glucose solution.	46
3.13	(a-b) CV measurements for different glucose concentrations and the (c-d) calibration plots of NiBT/Au film and Ni-BT/Au mesh respectively.	46
3.14	CV measurements of Ni(SC ₄ H ₉) ₂ /FTO at (a) different glucose concentrations (2.5- 4.8 mM) and its corresponding (b) calibration plot obtained from anodic peak current at each glucose concentration.	47
3.15	Sensitivity and Specificity towards glucose detection (a) Amperometric response of (a) Ni-BT/Au mesh and (b) Ni-BT/FTO at 0.6 V towards the successive addition of glucose of different concentrations in 0.1 M NaOH. (c) Calibration plot for different concentration of glucose for Au film, Au mesh and FTO electrode. (d) Glucose detection range for the transparent Au mesh and FTO compared with different analytes/ body fluids available for glucose detection.	48
3.16	(a) I-t measurement and (b) CV measurements of Ni(SC ₄ H ₉) ₂ /Au film for sequential addition of interfering molecules of 0.1 mM concentration to 1 mM glucose in 0.1 M NaOH. No signification change is observed in the peak potential. This is followed by addition of 2 mM of glucose resulting in a anodic peak shift to 0.73 V versus Ag/AgCl.	49
3.17	(a) Bar graph representing the changes in current ratio ($\Delta I/I$)% with respect to the electrode derived from CV measurements with and without glucose. (b) Consecutive cyclic voltammetry measurements at 50 mV/s for stability test.	50
3.18	(a) Bar graph representing the changes in current ratio ($\Delta I/I$)% with respect to the electrode derived from CV measurements with and without glucose. (b) Consecutive cyclic voltammetry measurements at 50 mV/s for stability test.	50
4.1	Figure of merit, typical synthetic methods and development strategies involved in oxygen evolution reaction.	53
4.2	(a) UV-visible spectrum and (b) FTIR spectrum of Co-HDT complex in solution.	56
4.3	(a) Thermogravimetric analysis (TGA) of Co-HDT precursor at 10 °C/min in N ₂ atmosphere. (b) Particle size distribution of Co ₃ O ₄ from FESEM image analysis in Image J software.	56
4.4	(a) X-ray diffraction pattern, (b) Raman spectrum, (c) Transmission Electron Microscopy (TEM) image, (d) High Resolution Transmission Electron Microscopy (HRTEM) image and (e) Selected Area Electron Diffraction (SAED) pattern of Co ₃ O ₄ films prepared by thermolysis of Co-HDT at 350 °C in N ₂ atmosphere. (f) Energy Dispersive Spectroscopy (EDS) analysis of Co ₃ O ₄ .	57
4.5	(a) Schematic demonstrating the dip coating method adopted for the fabrication of functional electrode materials based on a Co ₃ O ₄ /CC system for OER.	57
4.6	FESEM images of (a-c) pristine carbon cloth.	58
4.7	(a-c) FESEM images of Co ₃ O ₄ /CC electrodes at different magnifications. (d-f) EDS mapping of Co K α , and O K α from carbon fibre coated with Co ₃ O ₄ .	58
4.8	(a) Full survey spectra, high-resolution spectra of (b) S 2p and (c) C 1s before and after electrochemical oxidation for 50 test cycles.	59
4.9	High resolution XPS spectra of (a,b) Co 2p and (c,d) O1s of Co ₃ O ₄ /CC before and after electrochemical testing (50 cycles) respectively.	60
4.10	OER activity from Co ₃ O ₄ /CC electrodes fabricated by single time dip coating in precursor of different concentrations of Co-HDT ink and annealing at 350 °C in N ₂ . (a) LSV curves and the variations in (b) Overpotential values corresponding to concentration of the solution (c) Tafel slope analysis and	60

	(d) EIS analysis.	
4.11	OER activity of Co ₃ O ₄ /CC electrodes fabricated by LbL assembly of Co-HDT and thermolysis at 350 °C in N ₂ . (a) LSV curves, (b) variations in overpotential values corresponding to dipping number in solution (c) Tafel slope analysis, (d) Nyquist plots.	61
4.12	(a) LSV curves of Co ₃ O ₄ -16/CC in 1 M and 0.1 M of KOH and NaOH. (b) Bar graphs representing the effect of concentration and alkaline medium on overpotential for Co ₃ O ₄ -16/CC electrode.	62
4.13	(a) Double-layer capacitance calculation and (b) Chronopotentiometry of Co ₃ O ₄ /CC electrodes for different loading density by dip coating compared with electrodes prepared by multiple dip coating with a constant loading density and Inset shows the HRTEM image of Co ₃ O ₄ particles embedded in the carbon matrix. Note that the running number in all legends corresponds to the dipping number.	62
4.14	Cyclic Voltammetry (CV) curves of (a) Co ₃ O ₄ -2/CC, (b) Co ₃ O ₄ -16/CC, and (c) Co ₃ O ₄ -48/CC at different scan rates in faradic region (d) Comparative CV curves of Co ₃ O ₄ -2/CC, Co ₃ O ₄ -16/CC, and Co ₃ O ₄ -48/CC in non-faradic range for relative specific capacitance.	63
4.15	(a) Thermo gravimetric analysis of Ni-BT. (b) X-ray diffraction pattern, (c-d) FESEM, (e) elemental mapping, and (f) HRTEM (Insets with magnified image and SAED pattern) on carbon cloth obtained after annealing Ni-BT in N ₂ at 350 °C.	64
4.16	OER activity from NiO/CC electrodes fabricated by single time dip coating in precursor of different concentrations of Co-HDT ink and annealing at 350 °C in N ₂ . (a) LSV curves and the variations in (b) Overpotential values corresponding to concentration of the solution.	65
4.17	(a) Tafel slope analysis and (b) EIS analysis of NiO/CC electrodes fabricated by single time dip coating in precursor of different concentrations of Co-HDT ink and annealing at 350 °C in N ₂ .	65
4.18	OER activity of NiO/CC electrodes fabricated by LbL assembly of Co-HDT and thermolysis at 350 °C in N ₂ . (a) LSV curves, (b) variations in overpotential values corresponding to dipping number in solution.	66
4.19	(a) Tafel slope analysis, (b) Nyquist plots of NiO/CC electrodes fabricated by LbL assembly of Co-HDT and thermolysis at 350 °C in N ₂ .	66
5.1	(a) Digital photographs of Ni-BT, Co-HDT and corresponding mixture ink (b) UV-visible spectra, (c) M-T (ZFC) curves and (d) XRD patterns, (e) Schematic representing the lamellar structure of Co-HDT compared with Co-HDT:Ni-BT (4:1) and (f) DSC thermograms.	69
5.2	Photograph of carbon cloth coated with Ni-Co ink (35 × 10 cm ²) demonstrating scalability of the synthesis process.	70
5.3	(a) Photograph of carbon cloth (35 × 10 cm ²) dip-coated in Ni-Co ink with schematic demonstrating the process steps involved in the overall fabrication of NCO on carbon cloth for OER. (b) XRD patterns of Ni-Co oxides are abbreviated as NCO-0, NCO-20, NCO-50, and NCO-100 based on Ni%. (Note * denotes non-indexable planes)	71
5.4	Thermogravimetric Analysis (TGA) of Co-HDT:Ni-BT of Co-HDT, 1:1, 4:1 and Ni-BT at 10 °C/min in N ₂ .	72
5.5	(a-b) Transmission Electron Micrograph (TEM) images of NCO-20 nanoplates (c) HRTEM image showing 422 planes (d-spacing ~1.65Å) obtained from a magnified area of the nanoplate. Inset shows corresponding i-FFT analysis. (d) SAED pattern. (e) EDS mapping (f) M-H curves at 300 K. Inset in f shows the magnified region.	72
5.6	Raman spectra of NCO-0, NCO-20, NCO-50, and NCO-100.	73
5.7	HRTEM image of NCO-20 nanoplates and its analysis alongside from 10 different areas.	74
5.8	M-H curves of NCO-0, NCO-20, NCO-50 and NCO-100 at 2 K.	74
5.9	(a) CV curves of pristine Co ₃ O ₄ (NCO-0/CC), NiO (NCO-100/CC) and NCO-20/CC at 10 mV/s in 1 M KOH.	75
5.10	(a) LSV curves at 5 mV/s, (b) Tafel plot, (c) Nyquist plot (d) Tafel slope versus total resistances, and (e) current density versus scan rate for C _{dl} calculation of	75

	NCO-0/CC, NCO-20/CC, and NCO-100/CC. (f) Chronopotentiometry at 10 mA/cm ² of NCO-20/CC.	
5.11	CV of Co-Ni oxides on carbon cloth (CC) with (a) NCO-0/CC, (b) NCO-20/CC (c) NCO-100/CC at different scan rates ranging between 10-120 mV/s.	76
5.12	High-resolution X-ray Photoelectron Spectroscopy (XPS) spectra of NCO-0/CC (Co ₃ O ₄), NCO-20/CC, and NCO-100/CC (NiO) after activation of electrodes by CV cycling. (a) Ni 2p (b) Co 2p and (c) O 1s core-level spectra.	77
5.13	Deconvoluted Ni 2p spectra of pristine NCO-20/CC electrode before CV cycling.	78
5.14	(a) Photograph of setup for magnetism induced OER measurements. (b) I-t at overpotential for increment and decrement in the current density with and without a magnetic field of 300 mT. (c) CV curves at 10 mV/s of last 4 consecutive cycles and (d) LSV measurements with and without an applied magnetic field of NCO-20/CC.	79
6.1	(a) Schematic demonstrating the NiCo ₂ O ₄ nanoplates formation on carbon cloth substrate (b-d) High-resolution TEM images with insets showing magnified images and Selected Area Electron Diffraction pattern of Co ₃ O ₄ , NiO, and NiCo ₂ O ₄ . (e) HAADF-STEM image and corresponding EDS maps of Co K-edge and Ni K-edge signals originating from NiCo ₂ O ₄ nanoplates.	84
6.2	FESEM image of (a) carbon cloth coated with NiCo ₂ O ₄ and corresponding (b) magnified image shows the dense film over carbon fibers.	85
6.3	Deconvoluted XPS spectra of Ni 2p and Co 2p of (a) NiO (b) Co ₃ O ₄ and (c-d) NiCo ₂ O ₄ , respectively.	85
6.4	(a-c) High-resolution O1s core level spectra of Co ₃ O ₄ , NiO, and NiCo ₂ O ₄ , respectively.	86
6.5	(a) Square Wave Voltammetry (SWV) of Co ₃ O ₄ /CC, NiO/CC and NiCo ₂ O ₄ /CC electrodes with 200 μM DA, 50 μM UA and mixture of DA (200 μM) and UA (50 μM) and corresponding (b) current response of electrodes for simultaneous detection of UA and DA. (c) EIS Nyquist plot of all electrodes. (d) CV at 10 mV/s and (e) SWV of NiCo ₂ O ₄ /CC with DA (200 μM) and UA (100 μM). The mixture of DA (200 μM) and UA (100 μM) is also included for simultaneous detection (f) Influence of electrolyte pH on oxidation peak potentials. (Note: y-scale is the same for all graphs and hidden for clarity).	87
6.6	(a-b) CV of NiCo ₂ O ₄ /CC in 10 μM DA and 10 μM UA with varying scan rates (30-300 mV/s) and its (c-d) corresponding plot of current densities versus square root of scan rate, respectively.	88
6.7	Variation in (a) peak current densities with pH, (b) peak potential with pH and (c) peak separation with pH in 50 μM DA and 200 μM UA.	89
6.8	Square Wave Voltammograms (SWVs) of (a) DA and (b) UA from 1 nM – 1000 μM concentration, (c) simultaneous detection with increasing biomolecules (DA and UA respectively) and corresponding (d) calibration plots on NiCo ₂ O ₄ /CC.	89
6.9	Simultaneous detection of (a) different concentrations of DA in the presence of 1 μM UA (b) different concentrations of UA in the presence of 1 μM DA and their corresponding (c-d) calibration plots.	91
6.10	(a and b) Amperometric current (i-t) response with the increasing concentration of DA and UA at 0.35 V and 0.45 V, respectively, with insets showing a magnified view of the low concentration region. (c and d) Calibration plots derived from i-t measurements with error bars derived from repeat measurements.	92
6.11	Selectivity test of NiCo ₂ O ₄ /CC electrode on successive addition of 5 μL of Na ⁺ , glucose, Zn ⁺ , K ⁺ , Mg ²⁺ , Ca ²⁺ and Cu ²⁺ (1 mM) as interfering species to 0.1 M solution of (a) DA and (b) UA in PBS at an applied potential of 0.35 V and 0.45 V, respectively.	93
7.1	Expanded polystyrene as pollutant.	95
7.2	(a) Schematic demonstrating steps for conversion of the sugar-polystyrene composite to graphitic carbon in the presence of Ni-butanethiolate ink as a catalyst.	98
7.3	(b) Schematic illustration of the mechanism involved in the formation of graphitic carbon.	98

7.4	XRD pattern of Ni catalyst obtained from thermolysis of Ni butanethiolate in 5% hydrogen.	99
7.5	(a) Raman spectra of SPC7, SPC8, SPC9, and SPC10. Deconvoluted Raman spectrum of (b) SPC7 (c) SPC8, respectively.	99
7.6	Thermogravimetric Analysis (TGA) of sugar (S), polystyrene (P), sugar polymer composite with (SPC) and without catalyst (SP), polymer catalyst (PC) in nitrogen at 10 °C/min.	100
7.7	(a) X-ray diffraction (XRD) patterns, (b) Fourier-Transform Infrared Spectroscopy (FTIR) spectra and (c) BET isotherms for specific surface area (SSA) determination, and (d) NLDFT pore size distribution analysis of SPC8H, SP8H, SPC8, and SP8 carbon samples.	101
7.8	Deconvoluted Raman spectra of pyrolyzed carbon, before and after its hydrogenation (a) without catalyst (SP8 and SP8H) and (b) with a catalyst (SPC8 and SPC8H).	102
7.9	(a,c) HRTEM images along with the magnified view and (b,d) Selected Area Electron diffraction (SAED) pattern of SPC8H and SP8H, respectively.	103
7.10	(a) HRTEM image and corresponding SAED pattern of SPC8 carbon. (b) Enlarged view of a Ni nanoparticle located in the sample and its corresponding ED pattern.	104
7.11	(a) I-V characteristics of SPC8H and SPC8 carbon. (b) Comparative CV curves of carbon material synthesized at different temperatures.	104
7.12	Comparative (a) cyclic voltammograms at a scan rate of 50 mV/s, (b) Current density (J) with respect to different scan rates at 0.4 V versus RHE, and (c) Goodness of fit (R^2) values for surface-controlled and diffusion-controlled process in SPC8H, SPC8, SP8H, and SP8 carbon electrodes. (d) Galvanostatic charge-discharge curves at 2 A/g of SPC8H, SPC8, SP8H, and SP8 carbon electrodes.	105
7.13	CV curves of (a) SP8, (b) SPC8, (c) SP8H, and (d) SPC8H carbon electrodes at different scan rates (10-100 mV/s).	105
7.14	Current density at 0.4 V versus RHE as a function of square-root of scan rate (v) ^{1/2} for SPC8H, SPC8, SP8H, and SP8.	106
7.15	(a) Variation in specific capacitance values at different current densities, (b) Nyquist plots (inset in b shows magnified Nyquist plot at high frequency) of SPC8H, SPC8, SP8H, and SP8 carbon electrodes.	106
7.16	GCD curves of (a) SP8, (b) SPC8, (c) SP8H and (d) SPC8H carbon electrodes at different current densities (1-2 A/g).	107
7.17	(a) Photograph of cut pieces of waste polystyrene plate used for converting to graphitic carbon for EDLC device fabrication. (b) CV at different scan rates, (c) GCD curves, (d) specific capacitance at different current densities, and (e) cyclic capacitance retention at 4 A/g for SPC8H-WP/CC carbon in two-electrode geometry. The insets show the 1 st and 10,000 th cycle of GCD measurement performed for the cyclic stability test.	108
7.18	Comparative CV curves at 10 mV/s for pristine carbon cloth (CC) and graphitic carbon on carbon cloth (SPC8H-WP/CC) supercapacitor devices.	108
7.19	GCD plots for SPC8H-WP/CC at (a) low (1-8 A/g) and (b) high (10-20 A/g) current densities.	109

List of Tables

<i>Figures</i>	<i>Table</i>	<i>Page no.</i>
1.1	A brief literature survey of Glucose Sensors fabricated using Ni based functional electrodes.	10
1.2	Literature comparison among cobalt-based OER systems.	12
1.3	Literature comparison among Ni-Co oxide catalyst-based OER systems.	14
1.4	Comparison of electrochemical sensors for simultaneous determination of DA and UA.	15
1.5	Literature survey of carbon-based EDLCs derived from waste polymers.	18
3.1	Comparison in performance parameters of the Ni(SC ₄ H ₉) ₂ functionalized Au film, Au mesh and FTO electrodes obtained from CV measurements.	47
3.2	Comparison in performance parameters of the Ni(SC ₄ H ₉) ₂ functionalized Au film, Au mesh and FTO electrodes obtained from I-t measurements.	49
5.1	Calculated values of onset potential, overpotential, Tafel slope, and net resistances.	77
5.2	Binding Energy (BE) values derived from deconvoluted XPS spectra of Co 2p, Ni 2p, and O 1s.	77
5.3	XPS peak ratio analysis of Ni 2p, Co 2p, and O 1s spectra of NCO-based electrocatalysts.	78
6.1	Binding Energy (BE) values derived from deconvoluted XPS spectra of Co 2p, Ni 2p, and O 1s.	86
7.1	Tabulation of parameters derived from Raman analysis.	102

List of Symbols

Symbol *Description*

I	Current
V	Voltage
R	Resistance
C	Capacitance
L	Liter
μ	Micro
n	Nano
A	Ampere
F	Farad
M	Molar
I	Intensity
θ	Theta
$^{\circ}$	Degree
λ	Wavelength
m	meter
K	Kelvin
Oe	Oersted
Ms	Saturation Magnetization
S	Surface Area
%	Percentage
Ω	Ohm
v	Scan rate
~	Approximately
F	Faradays Constant
n	Number of electrons
D	Diffusion Coefficient
R_s	Solution resistance
R_{ct}	Charge transfer resistance
σ	Standard Deviation
J	Current Density
T	Temperature
s	Seconds
\AA	Angstrom
d	Interplaner spacing
Z	Impedance
ϕ	Phase shift
Z'	Real component of Impedance
Z''	Imaginary component of Impedance

List of Abbreviations

Abbreviation *Full form*

Ph.D.	Doctor of Philosophy
Ni-BT	Ni butanethiolate
Co-HDT	Co Hexadecanethiolate
ITO	Indium Tin Oxide
FTO	Fluorine Doped Tin Oxide
LOD	Limit of Detection
EDLC	Electric Double layer capacitor
XRD	X-ray Diffraction
XPS	X-ray Photoelectron Spectroscopy
UV	UV-Visible Spectroscopy
FTIR	Fourier Transform Infrared Spectroscopy
BET	Bruner-Emmett- Teller
SAED	Selected Area Electron Diffraction
TEM	Transmission Electron Microscopy
HRTEM	High Resolution Transmission Electron Microscopy
SEM	Scanning Electron Microscopy
FESEM	Field Emission-Scanning Electron Microscopy
EDX	Energy Dispersive spectroscopy
DSC	Differential Scanning Calorimetry
TGA	Thermo Gravimetric Analysis
JCPDS	Join Commission on Powder Diffraction Sheet.
LBL	Layer By Layer
RHE	Reversible Hydrogen Electrode
BE	Binding Energy
CC	Carbon Cloth
AFM	Antiferromagnetic
ZFC	Zero Field Cooled
FC	Field Cooled
OER	Oxygen Evolution Reaction
TOF	Turn Over Frequency
NCO	Nickel-Cobalt Oxide
LSV	Linear Sweep Voltammetry
CV	Cyclic Voltammetry
SWV	Square Wave Voltammetry
UA	Uric Acid
DA	Dopamine
AA	Ascorbic Acid
CA	Chronoamperometry
CP	Chronopotentiometry
EIS	Electrochemical Impedance Spectroscopy
GCD	Galvanostatic Charge Discharge
I-t	Current -Time
PAHs	Polycyclic Aromatic Hydrocarbons
TPA	Transpolyacetylene
SSA	Specific Surface Area
NLDFT	Non Local Density Function Theory
I-V	Current -Voltage
LoQ	Limit of Quantification
WP	Waste polystyrene

